

# Enhancement of Spin Mixing Conductance in $\text{La}_{0.7}\text{Sr}_{0.3}\text{MnO}_3/\text{LaNiO}_3/\text{SrRuO}_3$ Heterostructures

Christoph Hauser, Camillo Ballani, Philipp Dürrenfeld, Frank Heyroth, Philip Trempler, Stefan G. Ebbinghaus, Evangelos Th. Papaioannou, and Georg Schmidt\*

Spin pumping and the effective spin-mixing conductance in heterostructures based on magnetic oxide trilayers composed of  $\text{La}_{0.7}\text{Sr}_{0.3}\text{MnO}_3$  (LSMO),  $\text{LaNiO}_3$  (LNO), and  $\text{SrRuO}_3$  (SRO) are investigated. The heterostructures serve as a model system for an estimation of the effective spin-mixing conductance at the different interfaces. The results show that by introducing a LNO interlayer between LSMO and SRO, the total effective spin-mixing conductance increases due to the much more favorable interface of LSMO/LNO with respect to the LSMO/SRO interface. Nevertheless, the spin current into the SRO does not decrease because of the spin diffusion length of  $\lambda_{\text{LNO}} \approx 3.2$  nm in the LNO. This value is two times higher than that of SRO. The results show the potential of using oxide interfaces to tune the effective spin-mixing conductance in heterostructures and to bring novel functionalities into spintronics by implementing complex oxides.

## 1. Introduction

The current research on charge-to-spin current conversion effects such as the spin-Hall effect (SHE) offers great potential for applications in the field of spintronics and spin-orbitronics.<sup>[1,2]</sup> Among many studies on magnetic metallic and dielectric materials for the most efficient charge-to-current conversion, oxides have attracted less attention. However, incorporating oxides into the spin current

research field can be advantageous due to their tremendous variety of properties (e.g., electronic transport, magnetism) that can be tuned by deposition parameters (e.g., stoichiometry,  $\text{O}_2$  pressure, strain) and that depend on the operation conditions (e.g., temperature, magnetic, and electric fields). Furthermore, many oxide materials have commensurate lattice constants with perovskite-like structure that allow for very smooth interfaces in oxide heterostructures and hence can lead to well-defined properties at these interfaces.

In this article, we investigate spin pumping and we calculate the effective spin-mixing conductance  $g_{\text{eff}}^{\uparrow\downarrow}$  at low temperatures in  $\text{La}_{0.7}\text{Sr}_{0.3}\text{MnO}_3/\text{LaNiO}_3/\text{SrRuO}_3$  (LSMO/LNO/SRO) heterostructures. LSMO


is a prominent oxide material with a rich phase diagram.<sup>[3]</sup> We use LSMO where a ferromagnetic metallic phase up to 370 K in bulk material<sup>[3]</sup> is observed. Also, the inherently bad-metallic<sup>[4]</sup> oxide SRO shows a paramagnetic to ferromagnetic transition around 155 K.<sup>[5]</sup> LNO, contrary to all other rare earth (R) nickelates  $\text{RNiO}_3$  with a metal-insulator transition<sup>[6]</sup> is known to remain in a paramagnetic conducting phase even at low temperature. Previous studies on the spin pumping and the inverse spin-Hall effect (ISHE) in LSMO/SRO bilayers<sup>[7]</sup> have shown that SRO layers were acting as a spin sink exhibiting an ISHE which is similar in magnitude to that of Pt but of opposite sign. Recently, Ghosh et al.<sup>[8]</sup> proved the Kondo effect and a quite strong magnetoresistance in LSMO/LNO/SRO trilayers. Using ferromagnetic resonance (FMR) at room temperature they observed an increase in damping.

Here, we demonstrate the influence of a LNO interlayer between LSMO and SRO on  $g_{\text{eff}}^{\uparrow\downarrow}$  of the different interfaces. The spin-mixing conductance  $g^{\uparrow\downarrow}$  is one of the key concepts in the spin current transport through interfaces<sup>[9]</sup> as it describes the transport of spins at the interface between a ferromagnet (FM) and a second layer made from a different material. It should be noted that according to Tserkovnyak et al.<sup>[9]</sup>  $g^{\uparrow\downarrow}$  only describes the transmission of said interface and is only a valid approach if the second layer is a perfect spin sink with very strong spin scattering. For a full description of the spin current in a multi-layer not only the transmission of all interfaces but also the spin diffusion and spin flip in each respective layer need to be considered, which is typically done by combining all properties in  $g_{\text{eff}}^{\uparrow\downarrow}$  instead of  $g^{\uparrow\downarrow}$ . Accordingly for a full understanding the value of  $g_{\text{eff}}^{\uparrow\downarrow}$  which is accessible in the experiment needs to be disentangled into the mentioned properties for the analysis.

C. Hauser, C. Ballani, Dr. P. Dürrenfeld, P. Trempler,  
Dr. E. T. Papaioannou, Prof. G. Schmidt  
Institute of Physics  
Martin-Luther University Halle-Wittenberg  
Von-Danckelmann-Platz 3, 06120 Halle, Germany  
E-mail: Georg.Schmidt@physik.uni-halle.de

Dr. F. Heyroth, Prof. G. Schmidt  
Interdisziplinäres Zentrum für Materialwissenschaften  
Nanotechnikum Weinberg  
Martin-Luther University Halle-Wittenberg  
Heinrich-Damerow-Str. 4, 06120 Halle, Germany

Prof. S. G. Ebbinghaus  
Institute of Chemistry  
Martin-Luther University Halle-Wittenberg  
Kurt-Mothes-Str. 2, 06120 Halle, Germany

 The ORCID identification number(s) for the author(s) of this article can be found under <https://doi.org/10.1002/pssb.201900606>.

© 2020 The Authors. Published by WILEY-VCH Verlag GmbH & Co. KGaA, Weinheim. This is an open access article under the terms of the Creative Commons Attribution License, which permits use, distribution and reproduction in any medium, provided the original work is properly cited.

DOI: 10.1002/pssb.201900606

A large  $g_{\text{eff}}^{\uparrow\downarrow}$  means a large spin current, and if the difference in chemical potential of spin-up and spin-down in the FM is caused by FMR, as in spin pumping experiments, it also means a larger damping of the resonance. However, the estimation of the spin-mixing conductance in spin pumping experiments for magnetic/nonmagnetic (NM) layer systems is not trivial. Usually the calculation is done by measuring the increase in damping and comparing it to the characteristic value of a single uncapped magnetic layer without the spin sink. This uncapped layer acts as a reference sample with no losses due to spin pumping. However, in most of the metallic magnetic layers a capping layer is needed. The capping can largely modify the damping properties of the magnetic layer, a fact that cannot be correlated to the investigated spin pumping. Furthermore, different factors can influence the estimation of the increase in damping as, for example, the emergence of a finite magnetic polarization in the NM layer in contact with a ferromagnetic layer,<sup>[10,11]</sup> the spin memory loss effect<sup>[12]</sup> or the two-magnon scattering effect.<sup>[13]</sup> This is the reason why in experiments typically  $g_{\text{eff}}^{\uparrow\downarrow}$  is determined. In our study, no capping layer is needed because the bare LSMO reference layer is stable in air. Our work focuses on the estimation of  $g_{\text{eff}}^{\uparrow\downarrow}$  in an oxide trilayer system.

Previous experiments in which spin pumping through oxide interlayers was investigated showed varying results. Starting from YIG/Pt bilayers it was found that the insertion of a number of oxide interlayers reduces the spin-pumping efficiency,<sup>[14]</sup> whereas the insertion of NiO<sup>[15]</sup> leads to an increase in the spin-pumping efficiency and the ISHE, at least for very thin interlayers. In our experiments, we observe that the presence of an LNO interlayer increases the damping and as a consequence also  $g_{\text{eff}}^{\uparrow\downarrow}$ . We derive the spin diffusion length for the interlayer LNO, as well as  $g_{\text{eff}}^{\uparrow\downarrow}$  for the trilayers and also extract the respective values for  $g_{\text{eff}}^{\uparrow\downarrow}$  for the two interfaces. Magnetization and Curie-temperatures are measured by SQUID magnetometry and the samples are structurally characterized by X-ray diffraction and transmission electron microscopy (TEM) to confirm the interface quality.

## 2. Sample Fabrication

The heterostructures are deposited on (001)-oriented strontium titanate SrTiO<sub>3</sub> (STO) substrates, which are TiO<sub>2</sub>-terminated by wet etching and annealing.<sup>[16]</sup> The deposition is done in a copper-sealed pulsed laser deposition (PLD) chamber with a background pressure lower than  $4 \times 10^{-8}$  mbar. For deposition, an excimer laser with a wavelength of 248 nm is used. The laser fluency is chosen as  $2.3 \text{ J cm}^{-2}$  per pulse and the repetition rate as 2 Hz. An oxygen partial pressure of 0.2 mbar for the LSMO (40 nm) and SRO (6 nm) layers, and 0.4 mbar for the LNO layers is applied. Deposition is done at a substrate temperature of 750 °C. After deposition the heterostructure is cooled down at  $5 \text{ K min}^{-1}$ . The heterostructure compositions and the thickness of each layer are summarized in **Table 1**. For a LSMO/Pt reference stack (sample R2) a 13 nm thick Pt layer is deposited via DC magnetron sputtering without breaking the vacuum. The samples are cut afterward into pieces with the size of  $2 \times 5 \text{ mm}^2$  to fit into the SQUID magnetometer and the sample holder for FMR spectroscopy investigation. For ISHE measurements, we deposited Ti(10 nm)/Au(150 nm), via lift-off process, on the edges of the respective samples.

**Table 1.** Prepared layer stacks. The given thicknesses are nominal values. Summarized results from FMR and SQUID measurements.

Name	LSMO [nm]	LNO [nm]	SRO [nm]	Pt [nm]	Damping $\alpha/10^{-3}$	$M_{\text{eff}}/10^5$ [A m <sup>-1</sup> ]	$M_s/10^5$ [A m <sup>-1</sup> ]	$g_{\text{eff}}^{\uparrow\downarrow}/10^{20}$ [m <sup>-2</sup> ]
R1	40	–	–	–	$2.0 \pm 0.1$	$6.8 \pm 0.1$	$4.2 \pm 0.1$	–
R2	40	–	–	13	$20.0 \pm 3.0$	$6.9 \pm 0.3$	$4.4 \pm 0.2$	$2.11 \pm 0.53$
R3	40	3	–	–	$11.0 \pm 1.0$	$3.8 \pm 0.2$	$3.9 \pm 0.2$	$0.91 \pm 0.13$
S1	40	0	6	–	$3.1 \pm 0.4$	$7.5 \pm 0.2$	$4.7 \pm 0.1$	$0.14 \pm 0.04$
S2	40	1.8	6	–	$7.6 \pm 1.3$	$6.7 \pm 0.3$	$3.8 \pm 0.2$	$0.57 \pm 0.18$
S3	40	3	6	–	$13.0 \pm 2.0$	$4.1 \pm 0.2$	$4.4 \pm 0.2$	$1.16 \pm 0.26$
S4	40	6	6	–	$3.4 \pm 0.3$	$7.5 \pm 0.8$	$4.8 \pm 0.2$	$0.17 \pm 0.20$
S5	40	9	6	–	$10.4 \pm 1.7$	$6.4 \pm 0.1$	$4.1 \pm 0.1$	$0.93 \pm 0.19$
S6	40	11	6	–	$12.0 \pm 2.0$	$5.2 \pm 0.1$	$4.1 \pm 0.1$	$1.12 \pm 0.19$
S7	40	23	6	–	$19.0 \pm 1.9$	$3.2 \pm 0.1$	$2.4 \pm 0.1$	$1.11 \pm 0.20$

## 3. Structural Characterization

For all samples, structural characterization is done by X-ray diffraction and reflectometry. For sample S3, also high-resolution transmission electron microscopy (HRTEM) was performed. For X-ray characterization we use a Bruker D8 diffractometer with focused CuK<sub>α1</sub> radiation. For the detection, a scintillation detector is used in an unlocked  $\omega/2\theta$  scan of the (002)-reflection. **Figure 1a** shows, as an example, the results for sample S3. Simulations for fully strained layers yield out-of-plane lattice constants of  $c_{\text{LSMO}} = 3.858 \text{ \AA}$ ,  $c_{\text{LNO}} = 3.730 \text{ \AA}$ , and  $c_{\text{SRO}} = 3.972 \text{ \AA}$  for our layer stacks. The dashed lines in **Figure 1a** mark the positions of the respective peaks for fully pseudomorphic materials as a guide to the eye. According to these results, diffraction peaks on the left-hand side of the STO substrate (002)-peak (cubic lattice constant<sup>[17]</sup>  $a_{\text{STO,bulk}} = 3.905 \text{ \AA}$ ) must stem from SRO. On the right-hand side, the diffraction peaks of the layers with smaller lattice constant, namely LSMO and LNO appear. Due to the thinness of the LNO and SRO layers, only a prominent peak for the LSMO layer is visible. The presence of thickness fringes indicates smooth interfaces.

A simulation with thicknesses of  $d_{\text{LSMO}} = 39.1 \text{ nm}$ ,  $d_{\text{LNO}} = 2.5 \text{ nm}$ , and  $d_{\text{SRO}} = 5.5 \text{ nm}$  fits best the  $\omega/2\theta$  scan. The roughness of the surface and the interfaces calculated from X-ray reflectometry measurements is below 0.3 nm for all heterostructures. In **Figure 1b,c**, reciprocal space maps around the symmetric (002)- and asymmetric ( $\bar{1}03$ )-reflections are shown. As all layers have the same value for  $q_x$  in the measurement around the asymmetric ( $\bar{1}03$ )-peak, we can state that the heterostructure is fully strained and that the in-plane lattice constant for LSMO, LNO, and SRO is equal to  $a_{\text{STO}} = 3.905 \text{ \AA}$ . The  $\omega/2\theta$  scan (**Figure 1a**) is the line scan along  $q_x = 0$  for the measurement around the symmetric peak (**Figure 1b**).

For sample S3, a HRTEM image is made with a JEOL JEM 4010 electron microscope at an acceleration voltage of 400 kV. **Figure 2a** shows an image of the layer stack, which is cut in the (010)-direction (imaging is done along the (100)-direction). LSMO grows epitaxially with respect to the substrate and LNO is monocrystalline. For SRO, the first monolayers are also

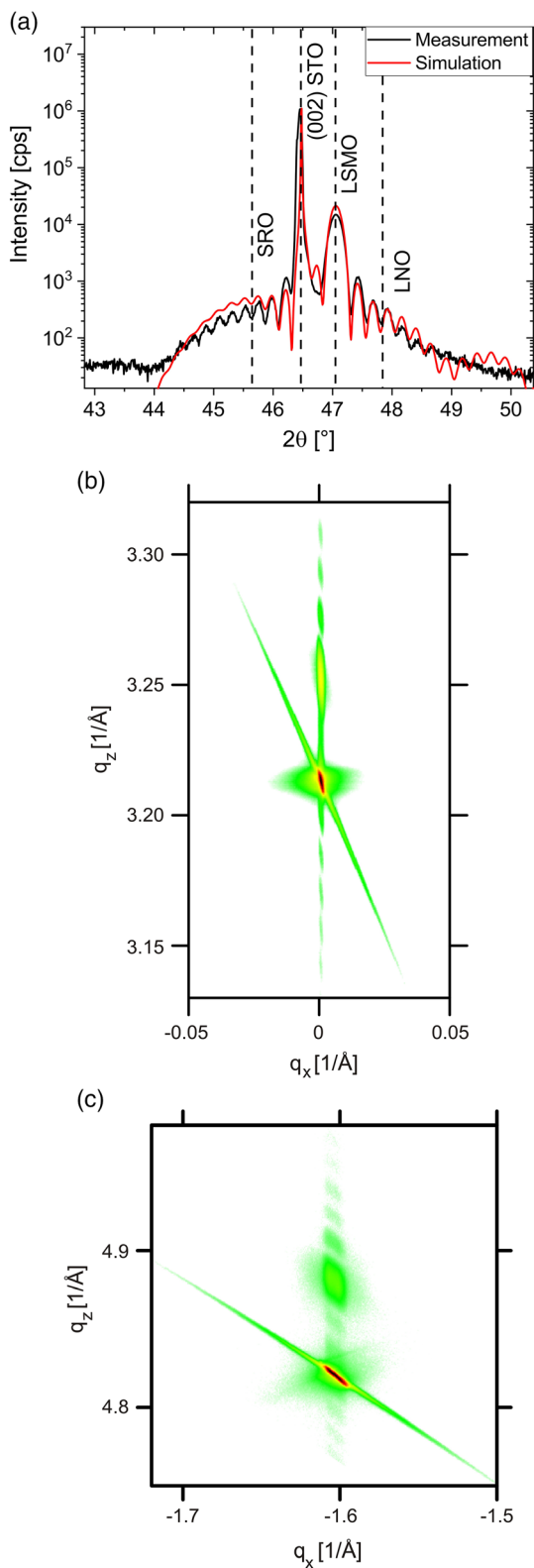


**Figure 1.** a)  $\omega/2\theta$  scan for the heterostructure LSMO(40 nm)/LNO(3 nm)/SRO(6 nm) (sample S3). The red curve is a fit to the data. b,c) Reciprocal space maps for sample S3 of the symmetric (002)- and the asymmetric  $(\bar{1}03)$ -peak, respectively. The heterostructure is fully strained.

epitaxial but apparently the rest of the layer is polycrystalline, as several orientations of the SRO crystal can be seen (Figure 2b). The interfaces are smooth and a very low interface roughness ( $<0.4$  nm) is observed. The thicknesses shown in Figure 2a match well the nominal thicknesses and the determined values

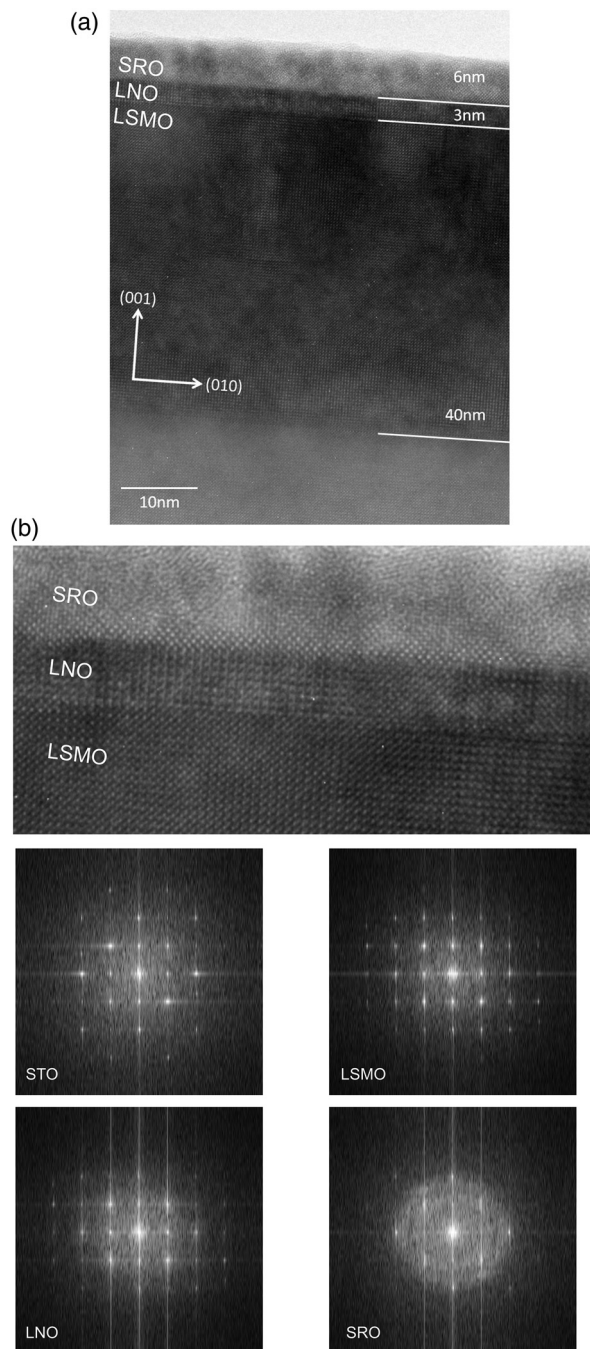


**Figure 2.** HRTEM measurement for sample S3 STO/LSMO(40 nm)/LNO(3 nm)/SRO(6 nm). a) Overview, b) zoom-in and FFT. The interfaces are smooth and LSMO and LNO appear monocrystalline, whereas for SRO several crystal orientations can be seen. The FFT of the layers show that indeed LSMO and LNO are epitaxial with respect to the substrate. SRO shows epitaxial and polycrystalline behavior.

from X-ray diffraction. We can thus estimate a deviation of less than 0.5 nm from the nominal thicknesses listed in Table 1. To prove the observed behavior, a fast Fourier transform (FFT) was done. It can be seen, according to the FFT, that LSMO and LNO are indeed grown epitaxial with respect to the substrate. The SRO on the other hand shows epitaxial as well as polycrystalline behavior as the appearance of gray rings in the FFT-image points out.

#### 4. SQUID Magnetometry

The magnetic characterization of samples R1, R3, and S3 is done with a Quantum Design SQUID VSM magnetometer. Here, we measure cooling curves and hysteresis loops for an LSMO/LNO (R3) layer stack and compare the results to the measurements for a bare LSMO layer (R1). For the investigation of the ferromagnetic phase transition of SRO, we additionally measure an LSMO/LNO/SRO heterostructure (S3). The cooling curves (Figure 3a) are measured at an external field of 1 mT along the (110)-direction of LSMO, which is the magnetic easy axis (according to our FMR experiments). The Curie temperature of LSMO for all samples is between 333 and 350 K, which is slightly lower than the value of 370 K for bulk material.<sup>[18]</sup> The drop of the magnetization below 105 K for sample S3 and R1 as well as the kink in the cooling curve of sample R3 at 105 K can be explained with the structural phase transition from cubic to tetragonal structure of the STO substrate at  $T = 105$  K.<sup>[19–21]</sup>

Angular dependence of the resonance field suggests a change in magnetic anisotropy of LSMO due to the phase transition of the STO (not shown here), which hence leads to a change in the measured magnetic moment. The kink at 135 K for sample S3 likely marks the ferromagnetic phase transition of SRO ( $T_C = 155$  K for bulk material<sup>[5,7]</sup>). In Figure 3b, hysteresis loops for samples R1, R3, and S3 are shown. The measurements are done with zero-field cooling, as this is also the way the FMR experiments are done. Here, the respective coercive fields for all three layer stacks are comparable and we do not observe any exchange bias. This is in contrast to Guo et al.<sup>[6]</sup> who found that bulk LNO becomes antiferromagnetic below 157 K if fabricated under certain deposition conditions and Sanchez et al.<sup>[22]</sup> and Peng et al.<sup>[23]</sup> who reported an exchange bias in LSMO/LNO bilayers below 50 and 100 K, respectively.

The saturation magnetization  $M_s$  for all samples is determined by SQUID magnetometry using hysteresis loops at 190 K along the (010)-direction of the LSMO. The values are shown in Table 1 and Figure 3c. As one can see, there is a slight variation in the  $M_s$  values. This is expected for LSMO due to the growth conditions. Although the thickness of the LSMO layer almost does not vary from sample to sample,  $M_s$  does. It is known that during the growth of LSMO layers and the annealing process structural deformations happen, as for example from lack of oxygen atoms, defects, or different stoichiometry. This results in variations in the  $M_s$  values.<sup>[24]</sup>

#### 5. FMR and Spin Pumping

FMR measurements and the investigation of the ISHE are performed in a cryostat at 190 K which, as shown previously,

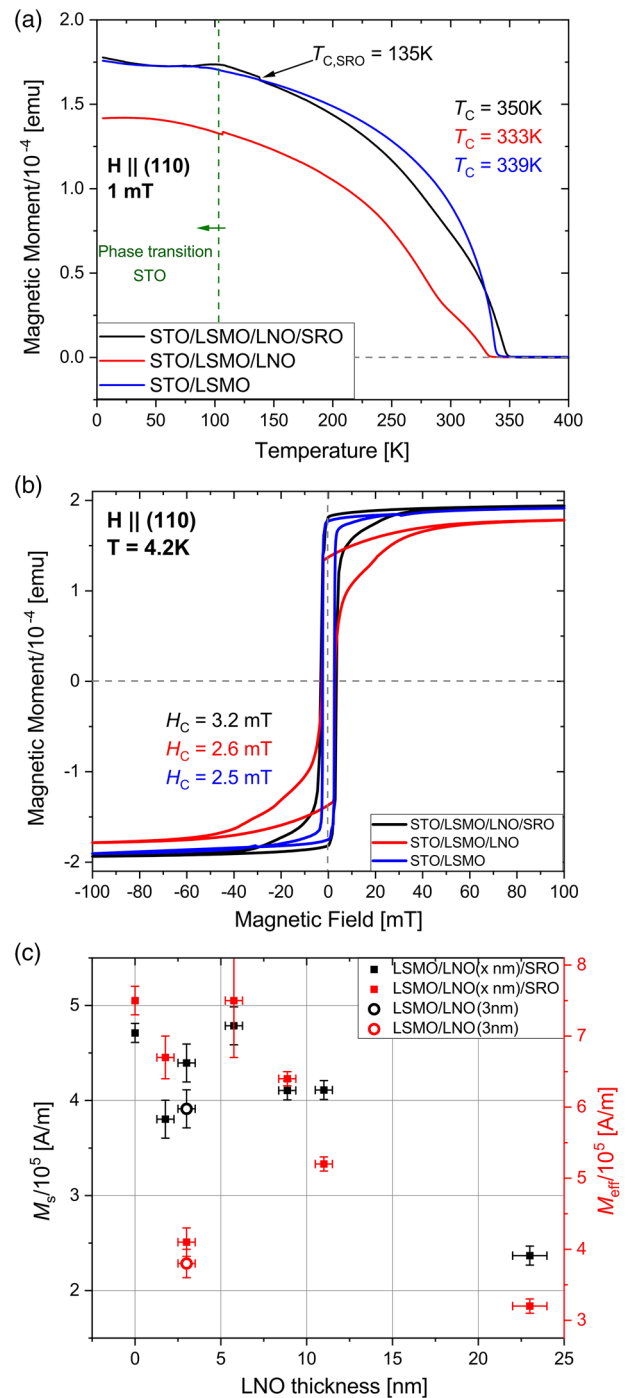


**Figure 3.** a) Cooling curves for a bare LSMO (sample R1 blue), a LSMO/LNO (sample R3 red), and LSMO/LNO/SRO (sample S3 black) heterostructure, respectively. The kink at 135 K likely relates to the phase transition of the SRO to the ferromagnetic state. b) Hysteresis loops of the three samples. The coercive fields are symmetric around zero for all samples. c) Saturation magnetization  $M_s$  and effective magnetization  $M_{\text{eff}}$  for sample R3 and S1–S7 at 190 K in (010)-direction of the LSMO.

is below the  $T_C$  of LSMO and above the  $T_C$  of SRO, to achieve spin pumping from a ferromagnetic into two paramagnetic layers. In addition, the choice of 190 K prevents a vanishing

ISHE in SRO as was observed at lower temperature by Wahler et al.<sup>[7]</sup> A RF current through a coplanar waveguide generates the necessary excitation field for FMR. To saturate the sample magnetization, a rotatable electromagnet generates a homogeneous external magnetic field aligned along the waveguide and along the (010)-direction of LSMO (in-plane,  $\phi = 0^\circ$ ), which is shown in Figure 4a.

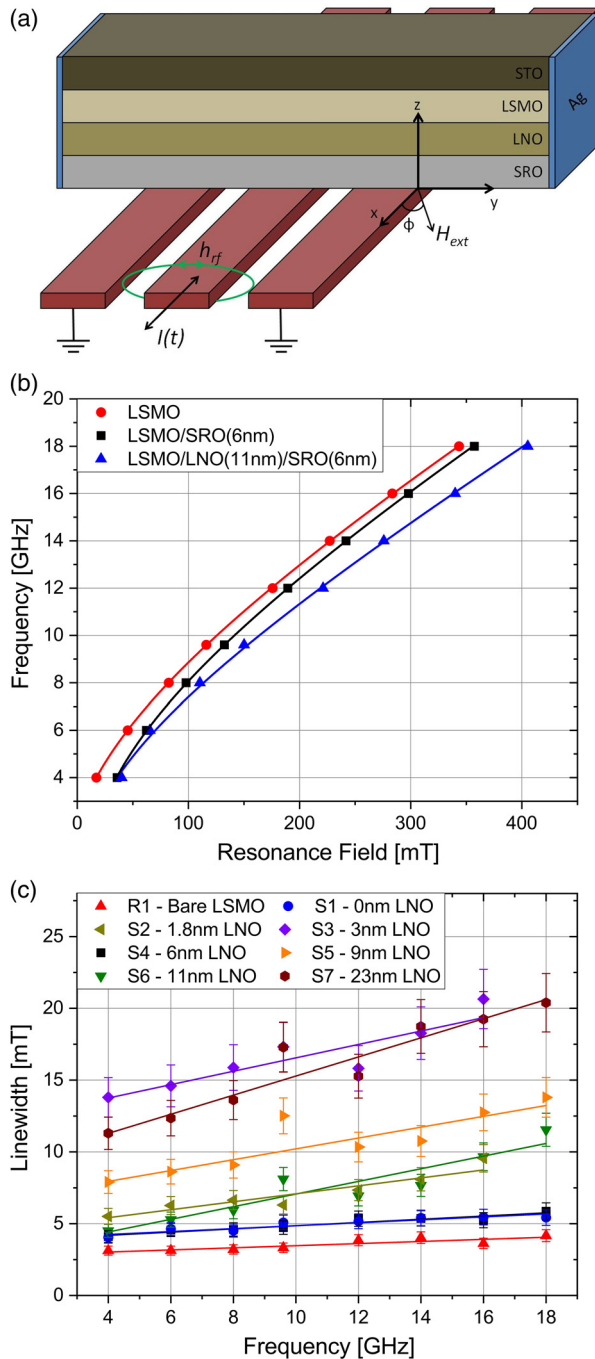


**Figure 4.** a) Measurement geometry for the FMR investigation. b) Resonance frequency in dependence of the resonance field. The lines are fits to Kittel's equation. c) FMR linewidth in dependence of the resonance frequency. The lines are linear fits to estimate the damping parameter  $\alpha$ .

For measuring FMR, a continuous-wave signal at constant frequency  $f$  in the range of 4–18 GHz is applied at a power of 10 dBm. The RF transmission is measured using a diode. The external magnetic field is modulated with 0.2 mT amplitude at a frequency of 20 Hz and lock-in technique is used to improve the signal-to-noise ratio.

The FMR field-swept measurements are fitted with a derivative of a Lorentzian function, which yields the half-width at half maximum FMR linewidth  $\Delta H_{\text{FMR}}$  and resonance field  $H_{\text{res}}$ .<sup>[25]</sup> With Kittel's equation<sup>[26]</sup>

$$f = \frac{\mu_0 \gamma}{2\pi} \sqrt{(H_{\text{res}} + H_{\text{ani}})(H_{\text{res}} + H_{\text{ani}} + M_{\text{eff}})} \quad (1)$$

we derive the gyromagnetic ratio  $\gamma$  and the effective magnetization  $M_{\text{eff}}$  from the dependence between  $f$  and the resonance field  $H_{\text{res}}$ .  $\mu_0$  and  $H_{\text{ani}}$  are the vacuum permeability and the anisotropy field, respectively. For  $\gamma/2\pi$  and  $\mu_0 H_{\text{ani}}$ , we derive values in the range of (27.5–28.5) GHzT<sup>-1</sup> and (2.4–33.9) mT, respectively. Indicatively, the results for samples R1, S1, and S6 are shown in Figure 4b. The damping parameter  $\alpha$  can be derived from a linear fit of the FMR linewidth  $\Delta H_{\text{FMR}}$  plotted over the RF-frequency<sup>[27]</sup>  $f$ :

$$\mu_0 \Delta H_{\text{FMR}} = \frac{2\pi\alpha f}{\gamma} + \mu_0 \Delta H_0 \quad (2)$$

where  $\mu_0 \Delta H_0$  is the inhomogeneous linewidth broadening. The values of  $\alpha$ ,  $\Delta H_0$ , and  $M_{\text{eff}}$  for all our heterostructures are summarized in Table 1 and damping measurements for samples R1 and S1–S7 are shown in Figure 4c. In our experiments, we see that the bare LSMO film (sample R1) exhibits the lowest damping ( $\alpha_{\text{LSMO}} = 2.0 \times 10^{-3}$ ). With any layer on top of LSMO that can act as a spin sink, the damping increases significantly, showing that the spin sink layers introduce additional channels for loss of angular momentum. Figure 5a shows the dependence of the damping as a function of the LNO interlayer thickness for samples S1–S7. The increase in damping in the heterostructures can be understood as the generated spin current carries angular momentum from the FM into the nonmagnetic interlayer (NM1) where it is either lost to the lattice by spin flip or diffuses further into the final spin sink (NM2). Due to conservation of angular momentum, a torque is created that decreases the precession angle and thus increases the damping in the FM. No clear trend of the damping in dependence of the LNO interlayer thickness can be observed here and an analysis only becomes viable when small variations of the saturation magnetization  $M_s$  are considered.

### 5.1. Spin-Mixing Conductance

When we do a full calculation of  $g_{\text{eff}}^{\uparrow\downarrow}$

$$\alpha_{\text{sp}} = \frac{g_{\text{eff}}^{\uparrow\downarrow} g_L \mu_B}{4\pi d_{\text{FM}} M_s} \quad (3)$$

( $g_L$ : g-factor,  $\mu_B$ : Bohr magneton, and  $M_s$ : saturation magnetization,  $d$ : layer thickness) using  $M_s$  as determined from SQUID-magnetometry and  $\alpha_{\text{sp}} = \alpha_{\text{sample}} - \alpha_{\text{LSMO}}$ , the dependence becomes visible. The derived values of  $g_{\text{eff}}^{\uparrow\downarrow}$  in the

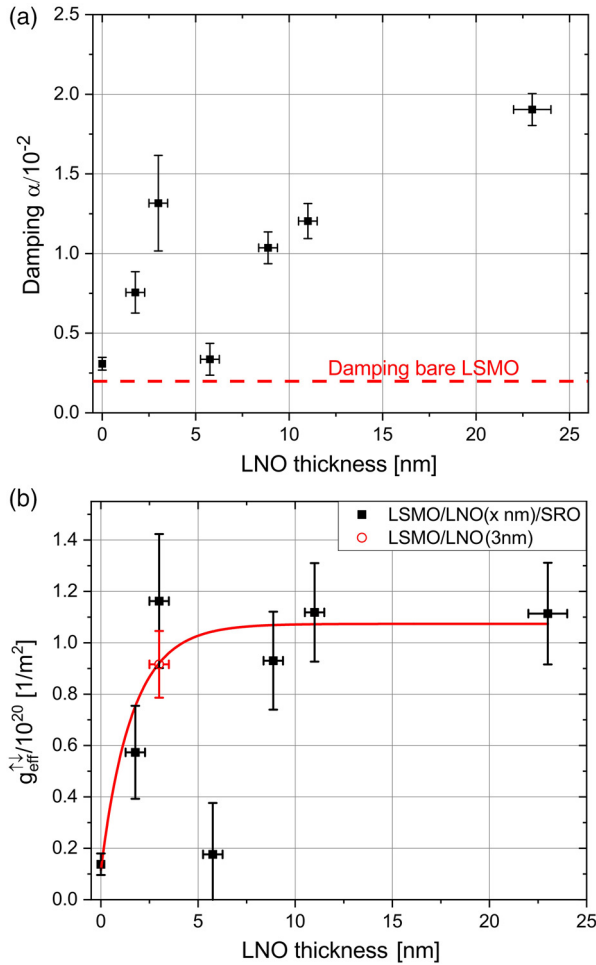


**Figure 5.** a) Damping and b) effective spin-mixing conductance  $g_{\text{eff}}^{\uparrow\downarrow}$  in dependence of the interlayer thickness in LSMO/LNO/SRO trilayers. The red line in (b) is a fit to the shown data and Equation (6). The fit reveals a spin diffusion length of  $\lambda_{\text{LNO}} = 3.2$  nm.

LSMO/LNO/SRO trilayers are depicted as a function of the LNO thickness in Figure 5b, showing a clear increase with LNO thickness and saturating at  $\approx 1.11 \times 10^{20} \text{ m}^{-2}$  for  $\approx 9$  nm LNO interlayer thickness.

To interpret our experiments, it is necessary to understand  $g_{\text{eff}}^{\uparrow\downarrow}$  in a trilayer system which has several contributions that may even influence each other. The spin-mixing conductance  $g^{\uparrow\downarrow}$  introduced by Brataas et al.<sup>[28]</sup> and Tserkovnyak et al.<sup>[9]</sup> only quantifies the spin transmission through the interface between the FM and the adjacent NM. To simplify a further discussion, we rename  $g^{\uparrow\downarrow}$  to  $g_{\text{FM}/\text{NM}}^{\uparrow\downarrow}$ . The quantity  $g_{\text{FM}/\text{NM}}^{\uparrow\downarrow}$  does not consider properties of the NM like conductivity or spin diffusion length. Only in the case where spins entering the NM layer are immediately flipped, this spin-mixing conductance alone needs to be considered for the additional damping by spin pumping as done by Tserkovnyak et al.<sup>[9]</sup> Starting from a bilayer system with immediate spin flip, we consider a model for the spin-mixing conductance, which is shown in Figure 6a. As soon as a spin accumulation appears in the NM, the spin flow through the spin-mixing conductance is reduced and the spin current is

no longer defined by  $g_{\text{FM}/\text{NM}}^{\uparrow\downarrow}$  but by  $g_{\text{eff}}^{\uparrow\downarrow}$ . In an equivalent circuit (Figure 6b), this can be implemented by adding a resistance  $R_{\text{sf},\text{NM}}$  between the spin accumulation ( $\mu^{\uparrow}$  and  $\mu^{\downarrow}$ ) in the NM, which represents the spin flip necessary to accommodate the steady state of one spin direction flowing into the NM and the other flowing back.

Only for immediate and complete spin flip this resistance is a short circuit leading back to  $g_{\text{eff}}^{\uparrow\downarrow} = g_{\text{FM}/\text{NM}}^{\uparrow\downarrow}$ . For a finite resistivity  $\sigma_{\text{NM}}$  and finite spin diffusion length  $\lambda_{\text{NM}}$ , the effective spin-mixing conductance  $g_{\text{eff}}^{\uparrow\downarrow}$  can be calculated from the additional damping in a bilayer system<sup>[29,30]</sup> for  $\lambda_{\text{NM}} \ll d_{\text{NM}}$  from Equation (3)

$$\frac{1}{g_{\text{eff}}^{\uparrow\downarrow}} = \frac{1}{g_{\text{FM}/\text{NM}}^{\uparrow\downarrow}} + R_{\text{sf},\text{NM}} \quad (4)$$

where the magnitude of the resistance  $R_{\text{sf},\text{NM}}$  depends on the spin flip time  $\tau_{\text{SF}}$  of the NM ( $\lambda_{\text{NM}} \propto \sqrt{\tau_{\text{SF}}}$ ) and only for a thickness of the NM ( $d_{\text{NM}}$ ) much bigger than  $\lambda_{\text{NM}}$  it has the fixed value of  $R_{\text{sf},\text{NM}} \propto \lambda_{\text{NM}}/\sigma_{\text{NM}}$ . For a thinner NM film, the so-called back flow needs to be considered and the more complex expression<sup>[9]</sup>

$$\alpha_{\text{sp}} = \left[ 1 + g_{\text{FM}/\text{NM}}^{\uparrow\downarrow} \frac{\tau_{\text{SF}} \delta_{\text{SD}}}{h \tanh(d_{\text{NM}}/\lambda_{\text{NM}})} \right]^{-1} \cdot \frac{g_{\text{L}} g_{\text{FM}/\text{NM}}^{\uparrow\downarrow} \mu_{\text{B}}}{4\pi d_{\text{FM}} M_{\text{s}}} \quad (5)$$

for the additional damping in a bilayer system needs to be used. Here  $\delta_{\text{SD}}$  is the energy level between two scattering states. Equation (3) is the limiting case of Equation (5) for large  $d_{\text{NM}}$ . In our experiments, the limit of  $\lambda_{\text{NM}} \ll d_{\text{NM}}$  is not yet reached and any addition of another layer will further increase  $g_{\text{eff}}^{\uparrow\downarrow}$ . In case a third layer (NM2) is added, the interface between NM1 and NM2 needs to be considered again in a similar way as for the first interface now adding the spin transmission  $g_{\text{NM1}/\text{NM2}}^{\uparrow\downarrow}$  to our picture (Figure 6c). Again we have to consider the layer properties of NM2 by adding  $R_{\text{sf},\text{NM2}}$ . The resulting additional damping  $\alpha_{\text{sp}}$  in a trilayer system can according to Tserkovnyak et al.<sup>[9]</sup> be written as

$$\alpha_{\text{sp}} = \left[ 1 + g_{\text{FM}/\text{NM1}}^{\uparrow\downarrow} \frac{\tau_{\text{SF}} \delta_{\text{SD}}}{h} \times \frac{1 + \tanh(d_{\text{NM1}}/\lambda_{\text{NM1}}) \tau_{\text{SF}} \delta_{\text{SD}} g_{\text{NM1}/\text{NM2}}^{\uparrow\downarrow}/h}{\tanh(d_{\text{NM1}}/\lambda_{\text{NM1}}) + \tau_{\text{SF}} \delta_{\text{SD}} g_{\text{NM1}/\text{NM2}}^{\uparrow\downarrow}/h} \right]^{-1} \times \frac{g_{\text{L}} g_{\text{FM}/\text{NM1}}^{\uparrow\downarrow} \mu_{\text{B}}}{4\pi d_{\text{FM}} M_{\text{s}}} \quad (6)$$

It should be noted that also in this equation Tserkovnyak et al.<sup>[9]</sup> assume immediate spin flip in the third layer so that only  $g_{\text{NM1}/\text{NM2}}^{\uparrow\downarrow}$  of the interface is relevant. Also in our case, the SRO ( $d_{\text{SRO}} = 6$  nm) is much thicker than the published value for the spin diffusion length in SRO<sup>[7]</sup> ( $\lambda_{\text{SRO}} = 1.5$  nm) and thus the backflow in the SRO can be neglected. For the limiting case of  $\lambda_{\text{NM1}} \ll d_{\text{NM1}}$ , the third layer should have no influence any more and indeed we find that in this limit the result of Equation (6) becomes identical to that of Equation (5) only with  $\lambda_{\text{NM1}} \ll d_{\text{NM1}}$  replaced by  $\lambda_{\text{NM}} \ll d_{\text{NM}}$ .

It should be noted that the introduced model (Figure 6) does not include a spin flip at the interface by scattering which would be associated with the so-called spin memory loss.<sup>[12]</sup> The equivalent circuit might be extended to include this effect but this will be described elsewhere.

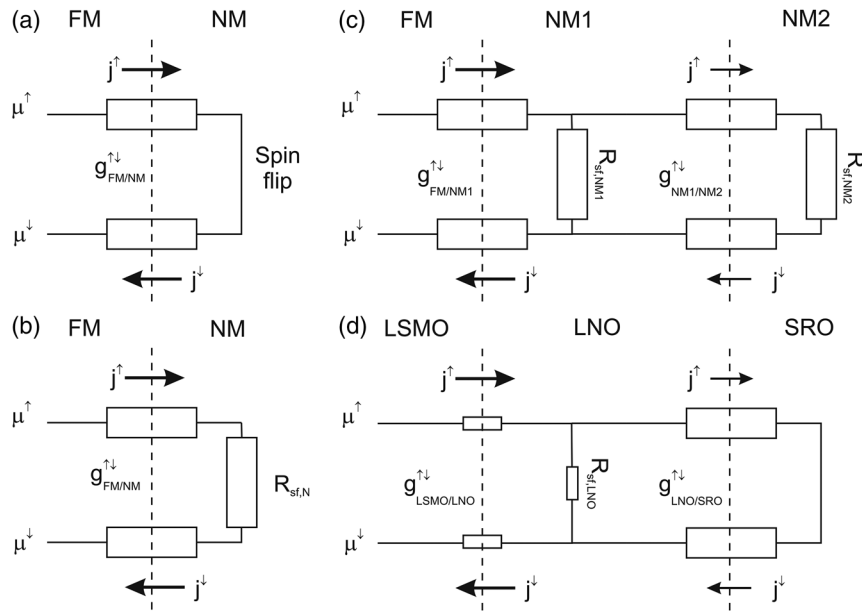


**Figure 6.** Schematic diagram of  $g_{\text{eff}}^{\uparrow\downarrow}$ . Due to the FMR, a spin accumulation is formed at the interface FM/NM which results in a splitting of the chemical potential  $\mu$  of  $\uparrow$ - and  $\downarrow$ -states. a) Model circuit for  $g_{\text{eff}}^{\uparrow\downarrow}$  in a bilayer system FM/NM in case of immediate spin flip in the NM. b) For finite spin diffusion length and resistance in NM, a spin flip resistance  $R_{\text{sf,NM}}$  has to be added. c) For trilayers FM/NM1/NM2, a second interface is generated with an additional spin sink NM2, which can be described using the interface transmission  $g_{\text{NM1/NM2}}^{\uparrow\downarrow}$  and a second spin flip resistance  $R_{\text{sf,NM2}}$ . d) In our LSMO/LNO/SRO trilayer,  $g_{\text{LSMO/LNO}}^{\uparrow\downarrow}$  and  $1/R_{\text{sf,LNO}}$  are both much larger than  $g_{\text{LNO/SRO}}^{\uparrow\downarrow}$ . This is pointed out by the size of the corresponding resistors (large  $g \rightarrow$  small  $R$ ).

## 5.2. Model for $g_{\text{eff}}^{\uparrow\downarrow}$ in LSMO/LNO/SRO

To fit the values of  $g_{\text{eff}}^{\uparrow\downarrow}$ , shown in Figure 5b, we use the following approach. As mentioned assuming immediate spin flip in the SRO is justified and only  $g_{\text{NM1/NM2}}^{\uparrow\downarrow}$  for the LNO/SRO interface,  $g_{\text{FM/NM1}}^{\uparrow\downarrow}$  for the LSMO/LNO interface and the spin flip and resistance of the LNO need to be considered. With  $g_{\text{eff}}^{\uparrow\downarrow} \propto \alpha_{\text{sp}}$ , we can use the following formula to fit the data

$$g_{\text{eff}}^{\uparrow\downarrow} = \left[ 1 + C_1 \cdot \frac{1 + \tanh(d_{\text{LNO}}/\lambda_{\text{LNO}})C_2}{\tanh(d_{\text{LNO}}/\lambda_{\text{LNO}}) + C_2} \right]^{-1} \cdot C_3$$

$$\text{with } \begin{cases} C_1 = g_{\text{LSMO/LNO}}^{\uparrow\downarrow} \frac{\tau_{\text{SF}}\delta_{\text{SD}}}{h} \\ C_2 = \frac{\tau_{\text{SF}}\delta_{\text{SD}}g_{\text{LNO/SRO}}^{\uparrow\downarrow}}{h} \\ C_3 = g_{\text{LSMO/LNO}}^{\uparrow\downarrow} \end{cases} \quad (7)$$

The fit results in a spin diffusion length of  $\lambda_{\text{LNO}} = (3.2 \pm 0.7)$  nm for LNO. This is in good agreement with the fact that for LNO thicknesses above 3 nm,  $g_{\text{eff}}^{\uparrow\downarrow}$  is no longer increasing and also matches the fact that (within error bars) the values of  $g_{\text{eff}}^{\uparrow\downarrow}$  are identical for LSMO/LNO(3 nm) and LSMO/LNO(3 nm)/SRO. One data point at an LNO thickness of 6 nm deviates for unexplainable reasons. It comes to mind that an oscillatory behavior due to quantum well states might be present;<sup>[31,32]</sup> however, the fact that our data points to a spin diffusion length well below 6 nm and that oscillating quantum well states have only been observed for much thinner layers mainly excludes this explanation.

For the fitting constants, we obtain  $C_1 = 0.85 \pm 0.19$ ,  $C_2 = 0.05 \pm 0.09$ , and  $C_3 = (2.20 \pm 0.41) \cdot 10^{20}$ , respectively. These values yield  $g_{\text{LSMO/LNO}}^{\uparrow\downarrow} = 2.2 \times 10^{20} \text{ m}^{-2}$  and  $g_{\text{LNO/SRO}}^{\uparrow\downarrow} = 1.2 \times 10^{19} \text{ m}^{-2}$ . The errors for the spin-mixing conductances are at least  $\pm 30\%$  if not more. In most experiments published on trilayers, the interlayer exhibits little spin flip while the spin sink (e.g., Pt) has a very high spin-mixing conductance. That case leads to  $g_{\text{NM1/NM2}}^{\uparrow\downarrow} > \frac{h}{\tau_{\text{SF}}\delta_{\text{SD}}}$  and an increase in thickness of the interlayer results in a decrease in  $g_{\text{eff}}^{\uparrow\downarrow}$ , as for example in FM/NM1/Pt trilayer systems.<sup>[9,30,33,34]</sup>

For LNO, however, the spin diffusion length is small, which combined with a large conductivity, leads to  $g_{\text{NM1/NM2}}^{\uparrow\downarrow} < \frac{h}{\tau_{\text{SF}}\delta_{\text{SD}}}$  and an increase in the effective spin-mixing conductance with increasing interlayer thickness.

The extracted values for  $g_{\text{eff}}^{\uparrow\downarrow}$  in the order of  $10^{20} \text{ m}^{-2}$  are relatively large. However, similarly large values for  $g_{\text{eff}}^{\uparrow\downarrow}$  have also been reported in literature for metallic system such as Co/Pt<sup>[35]</sup> in the range of  $4.5 \times 10^{19} \text{ m}^{-2}$  up to  $5.1 \times 10^{20} \text{ m}^{-2}$  as well as for YIG/Pt systems.<sup>[36]</sup> In our case, several factors can contribute to this large value. The LSMO/LNO interface has shown different kinds of magnetic coupling in the past and the strong paramagnetism of the LNO<sup>[37,38]</sup> may enhance the coupling beyond the ordinary transmission between a FM and a NM. In addition, the calculated  $g_{\text{eff}}^{\uparrow\downarrow}$  must be considered as an upper limit, valid only if there is no spin-memory-loss. If spins are lost at the interface, for example, by the two-magnon scattering mechanism<sup>[13,35]</sup> the measured value of  $g_{\text{eff}}^{\uparrow\downarrow}$  is higher than the model of Tserkovnyak et al.<sup>[9]</sup> would allow.

We can now compare the different contributions to  $g_{\text{eff}}^{\uparrow\downarrow}$ . When a 6 nm SRO layer is put on LSMO (sample R1  $\rightarrow$  sample S1)  $g_{\text{eff}}^{\uparrow\downarrow}$

increases from 0 to  $1.4 \times 10^{19} \text{ m}^{-2}$ . Adding 3 nm of LNO onto LSMO (sample R1  $\rightarrow$  sample R3) increases  $g_{\text{eff}}^{\uparrow\downarrow}$  from 0 to  $9 \times 10^{19} \text{ m}^{-2}$ . Thus, we assume that  $g^{\uparrow\downarrow}$  for LSMO/LNO is bigger than for LSMO/SRO. The ratio must even be more than 9:2, because we found that for 3 nm of LNO, the spins are not yet flipped completely but some backflow occurs. When SRO is added to the LSMO/LNO bilayer (sample R3  $\rightarrow$  sample S3), the increase of  $g_{\text{eff}}^{\uparrow\downarrow}$  is even identical within the error bars to the transition from pure LSMO to LSMO/SRO (sample R1  $\rightarrow$  sample S1). Additionally we can state, according to our fit of the effective spin-mixing conductance, that  $g_{\text{LSMO/LNO}}^{\uparrow\downarrow}$  is  $\approx 10$  – times bigger than  $g_{\text{LNO/SRO}}^{\uparrow\downarrow}$ , so that the transmission of spins at the LSMO/LNO is much more favorable than at the LNO/SRO interface.

This leads to the following picture for all parts of  $g_{\text{eff}}^{\uparrow\downarrow}$ : The interface contribution  $g_{\text{LSMO/LNO}}^{\uparrow\downarrow}$  is much larger than  $g_{\text{LSMO/SRO}}^{\uparrow\downarrow}$  for the LSMO/SRO bilayer.  $g_{\text{LNO/SRO}}^{\uparrow\downarrow}$  is similar to  $g_{\text{LSMO/SRO}}^{\uparrow\downarrow}$ . Because of the extremely short spin diffusion length in SRO, we can consider the connection between spin-up and spin-down channel in SRO as a short circuit, consistent with Equation (6). The spin diffusion length in LNO is comparable to the layer thickness so the spin-flip conductance  $1/R_{\text{sf,LNO}}$  has a finite value. However, from Figure 6b, it becomes clear that just because of Ohm's law, the values of  $1/R_{\text{sf,LNO}}$  and  $g_{\text{LSMO/LNO}}^{\uparrow\downarrow}$  both must be larger than  $g_{\text{eff}}^{\uparrow\downarrow}$  of the LSMO/LNO bilayer (because all three resistors are in series) and hence are also much larger than  $g_{\text{LNO/SRO}}^{\uparrow\downarrow}$ . In Figure 6d, this is depicted by the size of the different resistors (large  $g \rightarrow$  small R).

It is important to understand that the increase in  $g_{\text{eff}}^{\uparrow\downarrow}$  when a LNO interlayer between LSMO and SRO is introduced is mainly due to the spin-flip and the large conductivity of LNO. Even if the transmission through the LSMO/SRO interface were perfect ( $g_{\text{LSMO/LNO}}^{\uparrow\downarrow} \rightarrow \infty$ ), the insertion of the LNO layer would not increase  $g_{\text{eff}}^{\uparrow\downarrow}$  but mainly leave it constant because we know that  $g_{\text{LNO/SRO}}^{\uparrow\downarrow} = g_{\text{LSMO/SRO}}^{\uparrow\downarrow}$ . The increase only can occur if an additional spin flip channel is created inside the LNO layer. It should be noted that also spin memory loss at the LSMO/LNO interface might be a cause, but the evident dependence of  $g_{\text{eff}}^{\uparrow\downarrow}$  on the LNO thickness tells us otherwise. Our maximum values for  $g_{\text{eff}}^{\uparrow\downarrow}$  are higher than the recently published values of Ghosh et al.,<sup>[8]</sup> who estimated  $g_{\text{eff}}^{\uparrow\downarrow}$  in LSMO/LNO/SRO trilayers at room temperature. Most likely this is due to the increase in conductivity of the samples at lower temperature which increases  $g_{\text{sf,LNO}}^{\uparrow\downarrow}$ .

Because  $g^{\uparrow\downarrow}$  is related to the Sharvin resistance,<sup>[33]</sup> it is also understandable that its value increases with conductivity of the spin sink and the number of available conducting channels. This assumption is well in line with our results for sample R2 (LSMO/Pt) which has the highest  $g_{\text{eff}}^{\uparrow\downarrow}$  of all samples and the highest conductivity with a pure metal spin sink.

Finally, it should be noted that we also tried to measure the ISHE<sup>[39,40]</sup> in the different samples. We investigated the ISHE voltage for all fabricated samples by separating it from the anisotropic magnetoresistance effect<sup>[7,41–43]</sup> and thermo voltages.<sup>[44]</sup> Although no ISHE could be detected in an LSMO/LNO bilayer within the detection limit, we could identify a clear ISHE signal with the appropriate symmetry in the LSMO/LNO/SRO, proving that spin pumping into the SRO is taking place. Nevertheless,

as to be expected, the signals were extremely small and did not allow for a reasonable quantitative analysis.

## 6. Conclusion

We have shown that the insertion of a LNO layer between LSMO and SRO increases  $g_{\text{eff}}^{\uparrow\downarrow}$ . This effect can be linked to a highly transparent interface between LSMO and LNO and a large spin flip in the highly conducting LNO. Thickness-dependent measurements indicate a spin diffusion length of  $\approx 3.2$  nm, which is still twice as long as shown for SRO.<sup>[7]</sup>  $g^{\uparrow\downarrow}$  for LSMO/SRO and for LNO/SRO seem to be of similar magnitude. The increase for  $g_{\text{eff}}^{\uparrow\downarrow}$  leads to increased damping; however, only the outflow of spin current from the LSMO but not the inflow of spin current into the SRO is increased.

## Acknowledgements

This work was supported by the SFB 762. The authors thank the Max-Planck-Institut for microstructure physics for the access to transmission electron microscopy.

## Conflict of Interest

The authors declare no conflict of interest.

## Keywords

ferromagnetic resonance spectroscopy, oxides, spin mixing conductance, spin pumping

Received: September 26, 2019

Revised: February 7, 2020

Published online: March 18, 2020

- [1] J. Sinova, S. O. Valenzuela, J. Wunderlich, C. Back, *Rev. Mod. Phys.* **2015**, *87*, 1213.
- [2] A. Hoffmann, *IEEE Trans. Magn.* **2013**, *49*, 5172.
- [3] B. Cui, C. Song, G. Wang, Y. Yan, J. Peng, J. Miao, H. Mao, F. Li, C. Chen, F. Zeng, F. Pan, *Adv. Funct. Mater.* **2014**, *24*, 7233.
- [4] L. Klein, J. S. Dodge, C. H. Ahn, G. J. Snyder, T. H. Geballe, M. R. Beasley, A. Kapitulnik, *Phys. Rev. Lett.* **1996**, *77*, 2774.
- [5] G. Koster, L. Klein, W. Siemons, G. Rijnders, J. S. Dodge, C. B. Eom, D. H. A. Blank, M. R. Beasley, *Rev. Mod. Phys.* **2012**, *84*, 253.
- [6] H. Guo, Z. W. Lie, L. Zhao, Z. Hu, C. F. Chang, C. Y. Kuo, W. Schmidt, A. Piovano, T. W. Pi, O. Sobolev, D. I. Khomskii, L. Tjeng, A. C. Komarek, *Nat. Commun.* **2018**, *9*, 43.
- [7] M. Wahler, N. Homonnay, T. Richter, A. Müller, B. Fuhrmann, G. Schmidt, *Sci. Rep.* **2016**, *6*, 28727.
- [8] S. Ghosh, R. G. Tanguturi, P. Pramanik, D. C. Joshi, P. K. Mishra, S. Das, S. Thota, *Phys. Rev. B* **2019**, *99*, 115135.
- [9] Y. Tserkovnyak, A. Brataas, G. E. W. Bauer, *Phys. Rev. B* **2002**, *66*, 224403.
- [10] A. Conca, B. Heinz, M. R. Schweizer, S. Keller, E. T. Papaioannou, B. Hillebrands, *Phys. Rev. B* **2017**, *95*, 174426.
- [11] M. Caminale, A. Ghosh, S. Auffret, U. Ebels, K. Ollefs, F. Wilhelm, A. Rogalev, W. E. Bailey, *Phys. Rev. B* **2016**, *94*, 014414.



- [12] J. C. Rojas-Sánchez, N. Reyren, P. Laczkowski, W. Savero, J. P. Attaneé, C. Deranlot, M. Jamet, J. M. George, L. Villa, H. Jaffrés, *Phys. Rev. Lett.* **2014**, *112*, 106602.
- [13] A. Conca, S. Keller, M. R. Schweizer, E. T. Papaioannou, B. Hillebrands, *Phys. Rev. B* **2018**, *98*, 214439.
- [14] C. H. Du, H. L. Wang, Y. Pu, T. L. Meyer, P. M. Woodward, F. Y. Yang, P. C. Hammel, *Phys. Rev. Lett.* **2013**, *111*, 247202.
- [15] H. Wang, C. Du, P. C. Hammel, F. Yang, *Phys. Rev. Lett.* **2014**, *113*, 097202.
- [16] A. G. Schrott, J. A. Misewich, M. Copel, D. W. Abraham, Y. Zhang, *Appl. Phys. Lett.* **2001**, *79*, 1786.
- [17] H. Guo, S. Dong, P. D. Rack, J. D. Budai, C. Beekman, Z. Gai, W. Siemons, C. M. Gonzalez, R. Timilsina, A. T. Wong, A. Herklotz, P. C. Snijders, E. Dagotto, T. Z. Ward, *Phys. Rev. Lett.* **2015**, *114*, 256801.
- [18] A. Sadoc, B. Mercey, C. Simon, D. Grebille, W. Prellier, M. B. Lepetit, *Phys. Rev. Lett.* **2010**, *104*, 046804.
- [19] R. Loetzsch, A. Lübcke, I. Uschmann, E. Förster, V. Große, M. Thuerk, T. Koettig, F. Schmidl, P. Seidel, *Appl. Phys. Lett.* **2010**, *96*, 071901.
- [20] R. A. Cowley, *Phys. Rev.* **1964**, *134*, A981.
- [21] F. W. Lytle, *J. Appl. Phys.* **1964**, *35*, 2212.
- [22] J. C. R. Sanchez, B. Nelson-Cheeseman, M. Granada, E. Arenholz, L. B. Steren, *Phys. Rev. B* **2012**, *85*, 094427.
- [23] J. Peng, C. Song, F. Li, B. Cui, H. Mao, Y. Wang, G. Wang, F. Pan, *ACS Appl. Mater. Interfaces* **2015**, *7*, 17700.
- [24] A. A. Alharbi, M. Alkahtani, O. Al-Dossary, *AIP Conf. Proc.* **2011**, *1370*, 116.
- [25] Z. Celinski, K. B. Urquhart, B. Heinrich, *J. Magn. Magn. Mater.* **1997**, *166*, 6.
- [26] M. Liu, Z. Zhou, T. Nan, B. M. Howe, G. J. Brown, N. X. Sun, *Adv. Mater.* **2013**, *25*, 1435.
- [27] T. Liu, H. Chang, V. Vlaminck, Y. Sun, M. Kabatek, A. Hoffmann, L. Deng, M. Wu, *J. Appl. Phys.* **2014**, *115*, 17A501.
- [28] A. Brataas, Y. Tserkovnyak, G. E. W. Bauer, *J. Magn. Magn. Mater.* **2004**, *272*, 1981.
- [29] O. Mosendz, G. Woltersdorf, B. Kardasz, B. Heinrich, C. H. Back, *Phys. Rev. B* **2009**, *79*, 224412.
- [30] C. Du, H. Wang, F. Yang, P. C. Hammel, *Phys. Rev. Appl.* **2014**, *1*, 044004.
- [31] E. Montoya, B. Heinrich, E. Girt, *Phys. Rev. Lett.* **2014**, *113*, 136601.
- [32] A. M. Goncalves, F. Garcia, H. K. Lee, A. Smith, P. R. Soledade, C. A. C. Passos, M. Costa, N. M. Souza-Neto, I. N. Krivorotov, L. C. Sampaio, I. Barsukov, *Sci. Rep.* **2018**, *8*, 2318.
- [33] P. Deorani, H. Yang, *Appl. Phys. Lett.* **2013**, *103*, 232408.
- [34] L. Mihalceanu, S. Keller, J. Greser, D. Karfaridis, K. Simeonidis, G. Vourlias, T. Kehagias, A. Conca, B. Hillebrands, E. T. Papaioannou, *Appl. Phys. Lett.* **2017**, *110*(25), 252406.
- [35] L. Zhu, D. C. Ralph, R. A. Buhrmann, *Phys. Rev. Lett.* **2019**, *123*, 057203.
- [36] S. M. Rezende, R. L. Rodríguez-Suárez, M. M. Soares, L. H. Vilela-Leo, D. L. Domínguez, A. Azevedo, *Appl. Phys. Lett.* **2013**, *102*, 012402.
- [37] M. Tagliazucchi, R. D. Sanchez, H. E. Troiani, E. J. Calvo, *Solid State Commun.* **2006**, *137*, 212.
- [38] R. D. Sánchez, M. T. Causa, J. Sereni, M. Vallet-Regí, M. J. Sayagués, J. M. González-Calbet, *J. Alloys Compd.* **1993**, *191*, 287.
- [39] W. Zhang, M. B. Jungfleisch, W. Jiang, J. Sklenar, F. Y. Fradin, J. E. Pearson, J. B. Ketterson, A. Hoffmann, *J. Appl. Phys.* **2015**, *117*, 172610.
- [40] K. Harii, Z. Qiu, T. Iwashita, Y. Kajiwara, K. Uchida, K. Ando, T. An, Y. Fujikawa, E. Sautoh, *Key Eng. Mater.* **2012**, *508*, 266.
- [41] A. Azevedo, L. H. Vilela-Leao, L. Rodríguez-Suárez, A. F. L. Santos, S. M. Rezende, *Phys. Rev. B* **2011**, *83*, 144402.
- [42] N. Mecking, Y. S. Gui, C. M. Hu, *Phys. Rev. B* **2007**, *76*, 224430.
- [43] M. Obstbaum, M. Härtinger, H. G. Bauer, T. Meier, F. Swientek, C. H. Back, G. Woltersdorf, *Phys. Rev. B* **2014**, *89*, 060407.
- [44] K. Ando, E. Saitoh, *Nat. Commun.* **2012**, *3*, 629.